Transformations to amorphous and X-type phases in swift heavy ion-irradiated Ln_2O_3 and Mn_2O_3

View Online   Export Citation   CrossMark

Alexandre P. Solomon,[1] (iD) Cameron L. Tracy,[2] (iD) Eric C. O'Quinn,[1] (iD) Daniel Severin,[3] and Maik K. Lang[1,a] (iD)

AFFILIATIONS

[1]Department of Nuclear Engineering, University of Tennessee, Knoxville, Tennessee 37996, USA
[2]Belfer Center for Science and International Affairs, Harvard University, Cambridge, Massachusetts 02138, USA
[3]GSI Helmholtzzentrum für Schwerionenforschung, 64291 Darmstadt, Germany

[a]Author to whom correspondence should be addressed: mlang2@utk.edu

ABSTRACT

The intense, highly localized electronic excitation resulting from swift heavy ion irradiation induces phase transformations in many materials including lanthanide sesquioxides (Ln_2O_3). To explore the effects of chemical composition on radiation-induced transformations, the structural responses of several related sesquioxides to swift heavy ion irradiation were compared. Polycrystalline Nd_2O_3, Eu_2O_3, Yb_2O_3, and Mn_2O_3 were irradiated by 946 MeV Au ions to a range of ion fluences up to 2×10^{13} cm^{-2}, and structural modifications were characterized using beamline-based *in situ* x-ray diffraction and Rietveld refinement. Amorphization was induced in Nd_2O_3, Eu_2O_3, and Mn_2O_3 with the extent of induced transformation following a clear dependence on cation ionic radius. Nd_2O_3 and Eu_2O_3, having the largest cations, were rapidly amorphized, whereas Mn_2O_3, having the smallest cation, experienced only a slight loss of crystallinity at the highest fluences studied. The radiation response was different for Yb_2O_3, which underwent a sluggish transformation to a nonequilibrium X-type phase. The crystalline-to-amorphous transformations were proceeded by direct-impact mechanisms, while the C-to-X transformation was proceeded by a multi-impact mechanism.

I. INTRODUCTION

The process by which swift heavy ion (SHI) irradiation damages materials is fundamentally different from that of low-energy ions. For massive ions with specific kinetic energies in excess of ~1 MeV/u, energy is primarily deposited along the ion track by electronic excitation and ionization, rather than collisions with atomic nuclei. The densely excited electronic system subsequently dissipates the deposited energy through electron–electron and electron–phonon interactions. The latter transfers energy to the atomic system, causing a thermal spike that locally heats the material for a few picoseconds, followed by a rapid quench that typically leaves a modified atomic structure along the ion trajectory.[1–3] Swift heavy ion irradiation is of interest as a means of modifying materials in ways unachievable by conventional processing methods and for simulating the effects of fission fragment and alpha particle irradiation, which is useful for the development of improved nuclear materials.[4–6]

Energetic ion irradiation can produce unique defect configurations[7,8] and chemical changes in materials,[9,10] yielding structural modifications in a variety of oxides, including point and clustered defects,[11] amorphization,[12,13] and crystalline-to-crystalline phase transformations.[14–17] Understanding the fundamental mechanisms of radiation-induced structural modifications by characterizing the radiation responses of various materials enables the manipulation of these materials to obtain specific properties or engineered nanostructures.[18,19] Processing of Ln_2O_3 materials (where Ln refers to the lanthanides, La–Lu) in this way is particularly interesting due to their applications in a variety of technologies, including ultrafast and high-power solid-state lasers,[20,21] high-κ dielectrics,[22,23] catalysts,[24,25] nanoparticles for medical imaging,[26,27] and burnable neutron absorbers in nuclear fuels.[28] Desirable properties, such as enhanced ionic conductivity for solid oxide fuel cell (SOFC) electrolytes and reduced propagation losses in waveguides, can be tailored by inducing disorder while also enabling the recovery of nonequilibrium crystal phases to ambient conditions.[13,14,29]

Most materials in the Ln_2O_3 system are polymorphic, exhibiting different equilibrium crystal structures depending on temperature and pressure (Fig. 1). At atmospheric pressure and room

temperature, Ln_2O_3 compounds with large lanthanide ionic radii (Ln = La–Nd) preferentially adopt the trigonal A-type structure ($P\bar{3}m1$), in which cations are in sevenfold coordination with oxygen anions. All lanthanide sesquioxides with smaller cations (Ln = Pm–Lu) preferentially adopt the cubic C-type structure ($Ia\bar{3}$), characteristic of the mineral bixbyite, at ambient conditions.[30,31] The bixbyite unit cell can be described as a $2 \times 2 \times 2$ fluorite super-cell with ordered vacancies on one-quarter of the anion sites so that cations are in sixfold coordination with anions.[32]

Phase transformations induced in these materials by increasing temperature and pressure show similar dependence on lanthanide ionic radius. Those Ln_2O_3 materials with medium-sized cations (Ln = Sm–Ho) transform to the monoclinic B-type ($C2/m$) at elevated temperature or pressure. Additionally, most Ln_2O_3 materials transition further to a H-type ($P6_3/mmc$) phase at very high temperatures, and those with large cations adopt an X-type phase ($Im\bar{3}m$) within a narrow temperature range just below their melting point. The X-type unit cell has a body-centered cubic cation structure, yet the structure of the anions has been debated. Proposed anion sites include the $6b$ (50% occupancy), $12d$ (25% occupancy), and $24g$ sites (12.5% occupancy).[14,33] Due to this low occupancy of oxygen sites, X-type structures have been hypothesized to have high ionic conductivity typical of superionic conductors.[33] Because enhanced oxygen transport is of great importance for solid oxide fuel cells, X-type materials may prove to be excellent SOFC electrolytes.[34,35]

Ample investigations of the Ln_2O_3 system have explored both high-temperature and high-pressure polymorphs,[30,36–40] but recent research has extended the understanding of Ln_2O_3 polymorphism by using ion irradiation to induce various crystalline phase trans-formations. These studies have found that certain high-temperature or high-pressure polymorphs can be synthesized by intense ion irradiation and quenched to ambient conditions.[14,41–43] For example, Tang *et al.* observed transformations from the C-type to the B-type phase in Dy_2O_3 and Er_2O_3 irradiated with low-energy ions (300 keV Kr^{2+}) at cryogenic temperatures.[44] Using swift heavy

ions (185 MeV Xe and 2246 MeV Au), Tracy *et al.* and Lang *et al.* have induced both the C-to-B phase transformation and a transformation from the C-type to an amorphous phase in Ln_2O_3 materials with Ln = Sm–Ho.[14,45] Through the extreme conditions of SHI irradiation, far-from-equilibrium structures that are otherwise not accessible, such as the X-type phase shown in Fig. 1, have additionally been produced and quenched to standard temperature and pressure conditions.[14] Sattonnay *et al.* have also confirmed the C-to-B transformation for 1042 MeV Xe ion irradiation of Gd_2O_3 and Eu_2O_3, identifying a preferred crystallite orientation in the irradiation-induced phase.[46] The structural evolution and phase trans-formation behavior in irradiated Ln_2O_3 show a strong dependence on sesquioxide composition, ion energy, and ion energy loss.[14,43]

Previous SHI studies have not covered certain compositions in the lanthanide sesquioxide series, particularly those contain-ing relatively large lanthanide cations that form A-type phases, such as Nd_2O_3. High hygroscopy makes the measurements of irradiation-induced modifications in these materials especially chal-lenging, limiting the comparison of Ln_2O_3 materials with different size cations. Likewise, one of the sesquioxides featuring a much smaller lanthanide cation, Yb_2O_3, has not yet been characterized under SHI irradiation. This material is of interest for its probable transformation to the X-type phase.[14] Furthermore, the irradiation responses of isostructural, but chemically distinct, non-lanthanide sesquioxides such as Mn_2O_3 have not been thoroughly examined. The study of these materials is necessary to elucidate the funda-mental factors governing the radiation responses of this class of oxides and systematic trends in their phase behavior as a function of cation radius. Here, we report a detailed SHI irradiation study of A-type Nd_2O_3 (large lanthanide cation), C-type Eu_2O_3 (medium-sized cation), C-type Yb_2O_3 (small cation), and C-type Mn_2O_3 (isostructural with many Ln_2O_3 materials, but with a transi-tion metal cation) using 946 MeV Au ions. To facilitate the study of the highly hygroscopic A-type phase, structural modifications were measured using *in situ* x-ray diffraction (XRD) conducted *in vacuo*. SHI irradiation-induced material-dependent modifications include
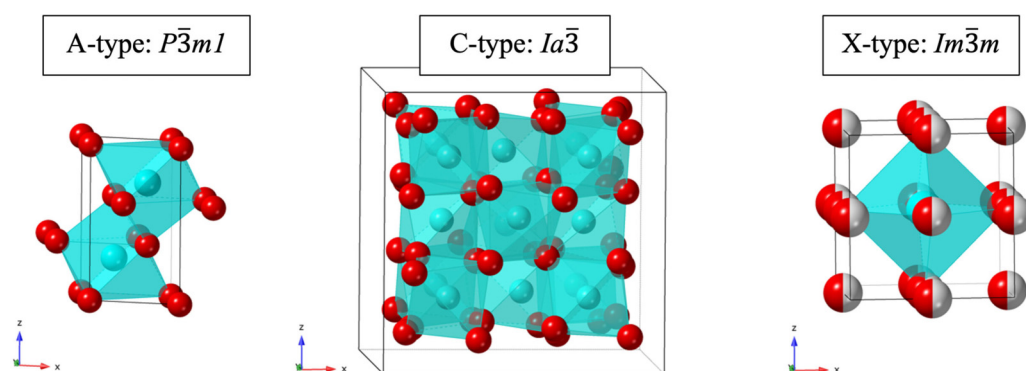

FIG. 1. Equilibrium crystal structures of Ln_2O_3-type materials at standard temperature and pressure (A-type and C-type) are represented in addition to the very high-temperature X-type phase, shown here with anions occupying the $6b$ site. At ambient conditions, the A-type phase exists for Ln = La–Nd and the C-type for Ln = Pm–Lu; the X-type exists for Ln = La–Dy above ~2300 °C. Transparent polyhedra indicate coordination between cations (blue spheres) and nearest neighbor anions (red spheres). Partial anion site occupancy is indicated by split red-gray spheres.

16 April 2024 01:32:28

a rapid amorphous transformation in both Nd_2O_3 and Eu_2O_3, a sluggish transformation to an X-type structure in Yb_2O_3, and a minor reduction of crystallinity in Mn_2O_3.

II. EXPERIMENTAL METHODS

Three lanthanide sesquioxide powders (Nd_2O_3, Eu_2O_3, and Yb_2O_3 purchased from Alfa Aesar with at least 99.9% purity) were first calcined at 800 °C for 50 h to remove any water present. Each powder was then pressed with a uniaxial pressure of 30 MPa to form a pellet with a diameter of 12 mm and a thickness of 3 mm. These pellets were sintered in air at 1100 °C for 30 h to densify and dehydrate. To prevent hydration, the Nd_2O_3 pellet was placed under vacuum immediately after sintering. MnO_2 powder (purchased from Alfa Aesar with at least 99.9% purity) was calcined and pressed under the same conditions as the lanthanide sesquioxides, but subsequent sintering differed; the pellet was sintered at 800 °C for 30 h in order to completely reduce the stoichiometry of the sample to Mn_2O_3.[47] XRD performed after sintering confirmed the crystalline phase of each sample and grain sizes greater than $1 \mu m$. The pellets were secured to copper sample holders for irradiation and *in situ* x-ray characterization.

Sample irradiation was performed at the M2 UNILAC beamline of the GSI Helmholtz Centre for Heavy Ion Research in Darmstadt, Germany. All pellets were irradiated with 946 MeV ^{197}Au ions at room temperature and under vacuum. The beam spot was scanned to ensure that the entire face of the pellet was irradiated to the desired ion fluence. To limit bulk heating of the sample, the gold ion flux was held below $1.8 \times 10^9 \, \mathrm{cm^{-2} \, s^{-1}}$. The samples were characterized by *in situ* XRD using a diffractometer integrated into the M2 beamline at the M-branch.[48] Measurements were performed before irradiation and after certain fluence steps (ranging from $10^{11} \, \mathrm{cm^{-2}}$ to $2 \times 10^{13} \, \mathrm{cm^{-2}}$) without removal of the samples from the beamline. These specific methods allowed for the characterization of Nd_2O_3, which adsorbs water so rapidly as to render *ex situ* measurement in air impracticable,[49] while enabling higher ion fluences to be reached.

The x-ray diffractometer installed at the M2 beamline is a custom-built 4-circle device with a $Cu-K_\alpha$ source in Bragg–Brentano geometry. One-dimensional XRD patterns were collected in the range of $2\theta = 25°–62°$ with collection times ranging from 40 to 80 s. The thickness of the damaged region was determined to be at least $27 \mu m$ in all four sesquioxides using the SRIM-2013 code.[50] The damaged region was much deeper than the penetration depth of the x rays, ensuring that only the irradiated portion of each pellet was probed, as 90% of the scattered intensity originated from the first $10 \mu m$ below the specimen surface.[48] Samples were exposed to the ion beam until each subsequent fluence step was achieved, and the XRD measurement was repeated. The extraneous signal was collected from the copper sample holders due to the relatively large size of the x-ray beam spot.

The XRD data were analyzed by Rietveld refinement[51] using GSAS II software.[52] Fits to the experimental data were obtained by refining the unit-cell parameters and microstrain based on peak shifts and peak broadening, respectively. Satisfactory fits were achieved for each material and fluence while subtracting the signal from the copper sample holder. Once refinement produced

fits of sufficient quality for the crystalline (B-type or C-type) A_2O_3 diffraction pattern, the refinements were modified to include the copper peaks. The diffraction peaks from the copper sample holder remained constant in intensity and position for each fluence step due to the high radiation tolerance of copper and the immobility of the sample holder in the *in situ* configuration. Thus, the copper XRD peaks served as an internal standard for quantitative analysis in the irradiated samples at various ion fluences. The crystalline phase fractions of the sample and the Cu standard reported by GSAS II were used to determine the fraction (by weight) of each crystalline and amorphous phase present in the samples by the conventional internal standard method.[53] Besides phase fractions, shifts in unit-cell parameters and evolution of microstrain were determined as a function of ion fluence for each sample composition.

III. RESULTS

In accordance with the phase diagram reported by Coutures *et al.*,[30] Ln_2O_3 materials with cation radii greater than ~ 0.97 Å preferentially adopt a trigonal ($P\bar{3}m1$) A-type structure at standard temperature and pressure. Those with smaller cation radii typically adopt a cubic ($Ia\bar{3}$) C-type structure, characteristic of the mineral bixbyite. Analysis of XRD patterns collected from the four materials prior to irradiation, displayed in Fig. 2, confirms that all samples exhibited the expected crystalline phases; the Nd_2O_3 pattern is representative of a phase pure A-type crystal structure, whereas the Eu_2O_3, Yb_2O_3, and Mn_2O_3 patterns indicate well-crystallized C-type structures with no impurity phases. No hydrous phases were present for Nd_2O_3, confirming that the sample treatment and experimental conditions were suitable to study this unstable compound.

The results of prior SHI irradiation experiments have indicated that amorphization, rather than a crystalline C-to-B phase transformation, can occur in C-type Ln_2O_3 materials (Sm–Er) below a threshold ion velocity (corresponding to some energy less than 2.2 GeV for Au ions).[14] Thus, transformation to either the B-type or an amorphous phase can be expected for irradiation by 946 MeV Au ions. With increasing ion fluence, Φ, the Nd_2O_3 and Eu_2O_3 patterns exhibit a gradual reduction in the intensity of all crystalline diffraction maxima accompanied by the appearance of broad, low-intensity bands [Figs. 2(a) and 2(b)]. One band is visible as a bump in Fig. 2(b) at about 25°–37°, although it is obscured by a low signal-to-noise ratio, and a similar low-intensity diffuse peak exists for irradiated Nd_2O_3. These broad bands result from diffuse scattering of x rays by amorphous sample domains lacking long-range periodicity.[57] Experiments using x rays from a laboratory source tend to produce a fairly weak signal from the amorphous phase as compared with synchrotron x rays, such that scattering from the amorphous volume is expected to be extremely weak in the diffraction pattern.[12,54–56] The gradual disappearance of crystalline peaks and the emergence of amorphous scattering bands indicate an irradiation-induced crystalline-to-amorphous transformation. Broadening of all crystalline peaks is evident and is explained by strain build-up and fragmentation of crystalline sample domains associated with the amorphization process. No new, sharp diffraction
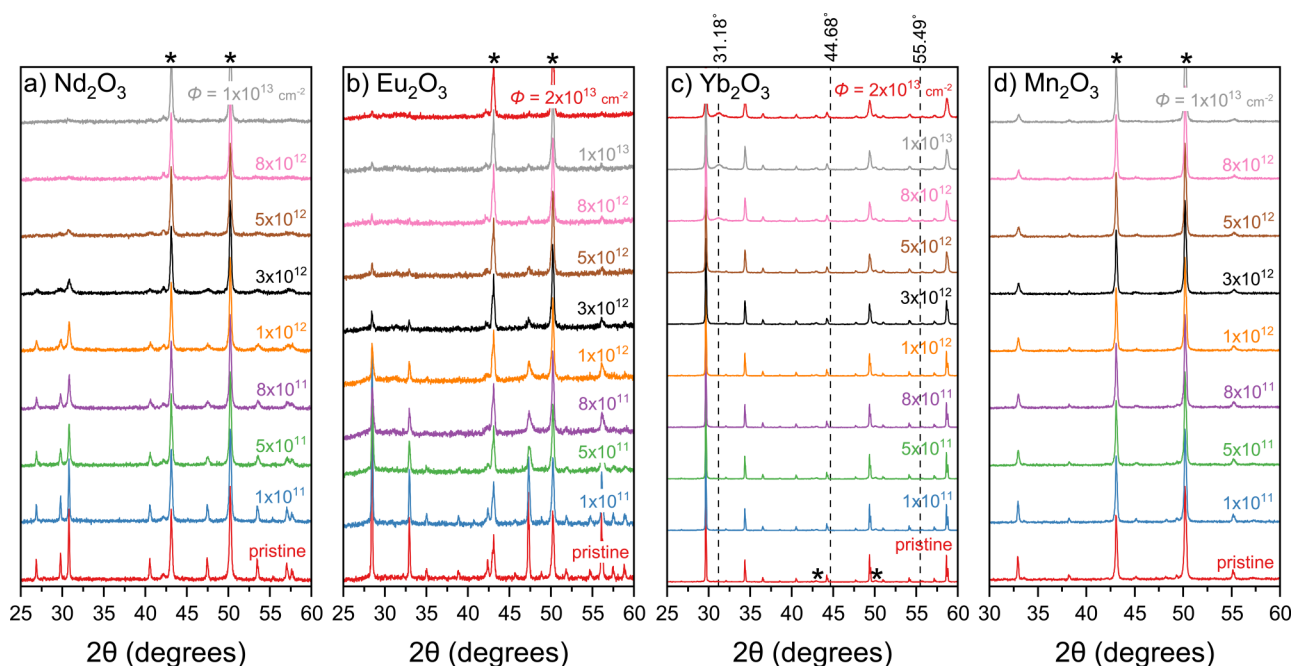
FIG. 2. Stacked XRD patterns shown for (a) Nd_2O_3, (b) Eu_2O_3, (c) Yb_2O_3, and (d) Mn_2O_3, pristine and irradiated with 946 MeV Au ions up to a fluence of 2×10^{13} ions/cm². Each pattern, except for those from Yb_2O_3, was normalized to the most intense copper diffraction peak. Bragg peaks marked with an asterisk correspond to copper from the sample holder.

maxima are seen in the XRD patterns for either Nd_2O_3 or Eu_2O_3, indicating that no well-crystallized B-type or other crystalline phase was formed by irradiation, which was confirmed by Rietveld refinement. The crystalline peak intensity of Eu_2O_3 diminishes more rapidly as a function of ion fluence than that of Nd_2O_3, indicating a larger amorphization cross section in the former. At a fluence of 10^{13} ions/cm², all crystalline peaks for both Nd_2O_3 and Eu_2O_3 have nearly disappeared, showing that both samples have become almost completely amorphous. As expected, the peak intensities from the copper sample holder remain constant throughout irradiation to all fluences.

The evolution of the Yb_2O_3 XRD patterns with ion fluence [Fig. 2(c)] exhibits an irradiation behavior markedly different from that of the previous two materials. Retention of the C-type peaks indicates that Yb_2O_3 largely maintains its initial structure up to a fluence of 2×10^{13} ions/cm², although a reduction in crystalline peak intensity is observed. Broadening of the crystalline diffraction peaks with increasing ion fluence can be attributed to strain from accumulated defects.[58] At fluences above 3×10^{12} ions/cm², two new diffraction features become visible in the patterns: a peak at 31.2° and a shoulder at 44.7° on the (431) C-type peak. These new peaks fit well to the X-type structure model (Fig. 1), which was observed previously in swift heavy ion-irradiated Tm_2O_3 and Lu_2O_3.[14]

XRD patterns of the Mn_2O_3 sample show retention of the initial C-type peaks up to the highest fluence, indicating that no distinct structural transformation is induced in this material by SHI

irradiation. All diffraction peaks reduce in intensity upon increasing fluence and show significant broadening that could be a consequence of defect formation or amorphization, although no diffuse scattering band is apparent up to 10^{13} ions/cm².

For the three materials whose XRD patterns clearly show large-scale irradiation-induced phase transformations (Nd_2O_3, Eu_2O_3, and Yb_2O_3), the loss of the starting phase and growth of the new phase as a function of ion fluence were analyzed to yield information about the phase transformation mechanisms. The crystalline phase fractions of amorphizable Nd_2O_3 and Eu_2O_3 for a given fluence were obtained by Rietveld refinement of XRD patterns representing the remaining C-type sesquioxide phase and the (constant) copper phase. Subtle diffuse scattering from the amorphous phase was subtracted with the background prior to the refinement. The crystalline phase fractions for both Nd_2O_3 and Eu_2O_3 decrease noticeably as a function of increasing ion fluence, at a much faster rate for Eu_2O_3, and appear to saturate at ~4% at higher fluences (Fig. 3). This behavior can be best described by a direct-impact (i.e., single-impact) model, which assumes that each incident ion produces an amorphous track along the ion's path and that no track overlap is required to create an amorphous region in the target material. An equation for the unmodified crystalline sample volume remaining after irradiation to a given fluence was derived from Poisson statistics. Because some small crystalline peaks persist even at the highest fluences studied, indicating possible saturation of the amorphous fraction, the direct-impact model was adjusted to allow non-zero crystalline fractions at high
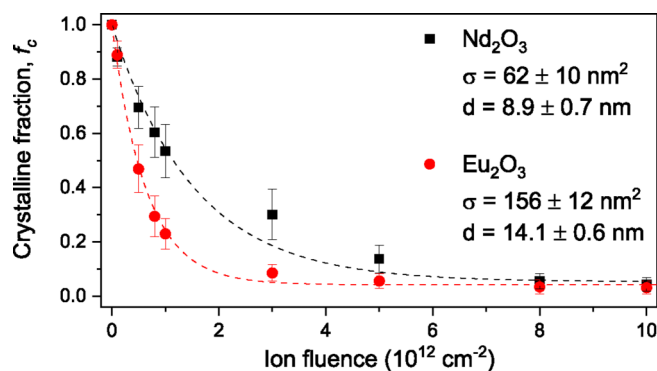
FIG. 3. Crystalline fraction by weight, f_c, obtained by the Rietveld analysis of XRD patterns, shown for Nd_2O_3 (black squares) and Eu_2O_3 (red circles) as a function of ion fluence. The dashed lines represent the fits to the experimental data based on Eq. (1). The amorphous track cross-sectional areas, σ (and associated track diameters, d, assuming cylindrical symmetry) extracted from the fits are reported. Error bars show uncertainty associated with the refinements.

fluences,[59]

$$f_c(\phi) = (1 - b)e^{-\sigma\phi} + b, \qquad (1)$$

in which f_c is the remaining crystalline fraction by weight, ϕ is the ion fluence, and σ is the cross-sectional area of the amorphous region of the ion track. The constant b represents the remaining crystalline fraction at infinite ion fluence. A Levenberg–Marquardt (damped least squares) fit was obtained for Eq. (1) and plotted alongside the refined remaining crystalline fractions in Fig. 3.

The crystalline fractions of both Nd_2O_3 and Eu_2O_3 are fit well by the direct-impact model described in Eq. (1). A multi-impact mechanism, wherein multiple ions must traverse a given volume of material in order for it to transform, would produce sigmoidal loss of the crystalline phase. Though a multi-impact mechanism has been observed for SHI irradiation-induced transformations in other binary oxides,[16] there is no evidence of sigmoidal behavior seen within the uncertainties of experimental data for Nd_2O_3 and Eu_2O_3. Track diameters of 8.9 ± 0.7 and 14.1 ± 0.6 nm were calculated from the cross-sectional area, σ, for Nd_2O_3 and Eu_2O_3, respectively; saturation values, b, deduced from Eq. (1) were 5% and 4%, respectively. As qualitatively observed from the XRD data in Fig. 2, the crystalline fraction of Eu_2O_3 decreased more distinctly with fluence than that of Nd_2O_3 (Fig. 3) due to the larger cross-sectional area of the amorphous ion tracks produced in Eu_2O_3.

In contrast to ion-beam-induced amorphization of Nd_2O_3 and Eu_2O_3, two new diffraction maxima are visible in the XRD patterns of Yb_2O_3 [Fig. 2(c)] and were indexed to the (110) and (200) peaks of the X-type phase. Rietveld refinement of the XRD patterns with mixed C-type and X-type phases provided a very good fit to the experimental data for each fluence, confirming that C-type Yb_2O_3 transforms to an X-type phase rather than an amorphous phase in response to SHI irradiation. Although X-type maxima are only visually apparent in the XRD patterns at fluences of 5×10^{12} ions/cm²

and higher, refinements indicated the accumulation of an X-type phase fraction at lower fluences [Fig. 4(a)]. The X-type phase fraction, f_X, increases with ion fluence after an initial latent period and appears to saturate at the maximum fluence at $f_X = \sim 15\%$. The pronounced sigmoidal growth of the X-type phase fraction with increasing ion fluence indicates a multi-impact mechanism. This means that multiple ion tracks must overlap to induce C-to-X transformation in Yb_2O_3,[60] suggesting a stepwise transformation process wherein structural defects produced by previous ion impacts facilitate a gradual transformation of a given volume of material.

Microstrain in Yb_2O_3, determined from "peak broadening" through Rietveld refinements of the remaining C-type phase, reveals a correlation with the onset/saturation of X-type phase formation, illustrating the role that defect accumulation and structural distortion play in this transformation process [Fig. 4(b)]. With increasing ion irradiation, the microstrain accumulates monotonically at three distinct rates of increase, as indicated by the linear slope lines in Fig. 4(b). The initial accumulation of microstrain at low ion fluences is rapid as (largely isolated) point defects and small defect clusters are produced up to a fluence of $\sim 3 \times 10^{12}$ ions/cm², at which point the rate of accumulation decreases. Above this fluence, defect-rich ion tracks begin to
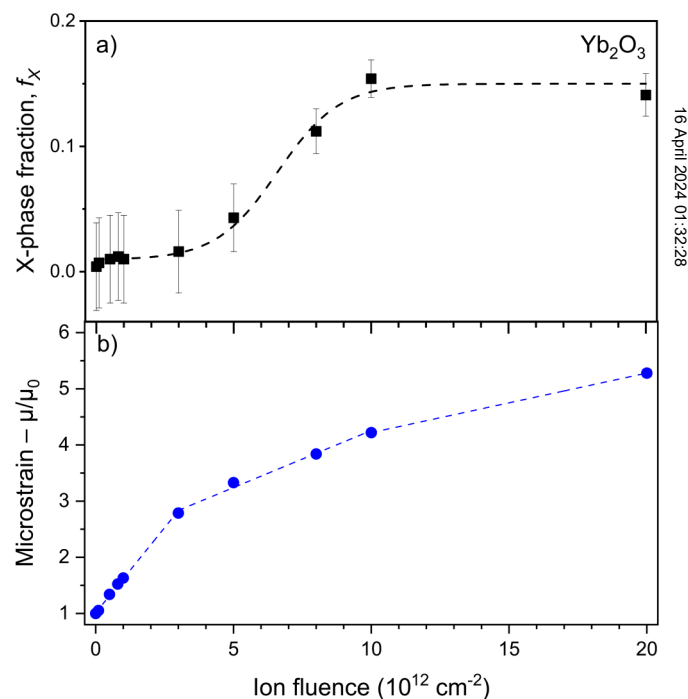

FIG. 4. (a) X-type phase fractions by weight, f_X, of irradiated Yb_2O_3 vs ion fluence as obtained by Rietveld refinement of XRD patterns. A sigmoidal fit has been added to qualitatively suggest a trend in the X-type fraction, indicating saturation at ~15%. (b) Microstrain of C-type Yb_2O_3 determined by the Rietveld analysis of XRD patterns measured at each ion fluence with dashed lines indicating the distinct rates of increase. Error bars shown represent the error associated with the refinements; they are smaller than the symbol for (b).

overlap, and diffraction maxima of the X-type phase become visible in the XRD patterns [Fig. 2(c)]. The accumulation rate further decreases at a fluence of $\sim 10^{13}$ ions/cm^2 as the X-type fraction nears saturation. Saturation of the X-type fraction below unity implies a steady-state regime of ion-beam-induced X-type phase formation and replacement by the C-type phase in the absence of any detectable amorphization.

Figure 5(a) presents stacked XRD patterns for Yb$_2$O$_3$ in detail with increasing ion fluence, emphasizing the emerging (110) X-type peak at fluences greater than 3×10^{12} ions/cm^2. The C-type structure remains mostly intact, and there is no evidence of amorphization or transformation to the B-type phase, as commonly observed in sesquioxides with larger lanthanide elements. The inset reveals a polytonic shift in C-type peak positions, shown for the (222) peak, and a gradual increase in peak width. This most intense C-type diffraction maximum exhibits complex behavior in 2θ position during irradiation, corresponding to both unit-cell contraction and expansion.

The shift of the C-type Yb$_2$O$_3$ unit-cell parameter indicates a complex interplay between irradiation-induced defect accumulation within the C-type matrix and stresses induced by X-type domain formation. The initial expansion of the unit cell [Fig. 5(b)] is interpreted as swelling from the production of defects, corresponding to the pronounced buildup of microstrain at low fluences [Fig. 4(b)]. The contraction that follows at higher fluences may be explained by the formation of X-type domains, which are less dense than the
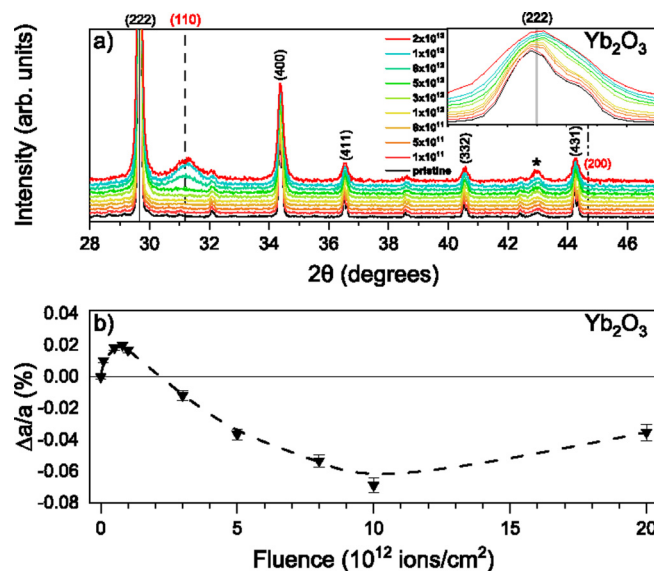
C-type phase per the X-type phase model (Fig. 1),[14] exerting compressive stresses on the remaining C-type volume.[55] The reversion to unit-cell expansion at the highest fluences achieved "coincides" with the saturation of the X-type fraction. This suggests that defect accumulation in the remaining C-type volume persists after X-type creation and removal has reached steady state, which is in agreement with the continued increase in microstrain across the same fluence range [Fig. 4(b)]. These distinct polytonic trends observed in X-type phase fraction as well as in C-type microstrain and unit-cell parameter provide further evidence of a multi-impact transformation mechanism in Yb$_2$O$_3$. The transformation to the X-type phase appears to be driven by the accumulation of a critical defect density that is reached after multiple ion impacts, in agreement with previous studies on other binary oxides.[16]

No new crystalline phases were observed in the irradiated Mn$_2$O$_3$ [Fig. 2(d)]. Instead, minor amorphization is indirectly evident based on the reduction in peak intensity with no apparent
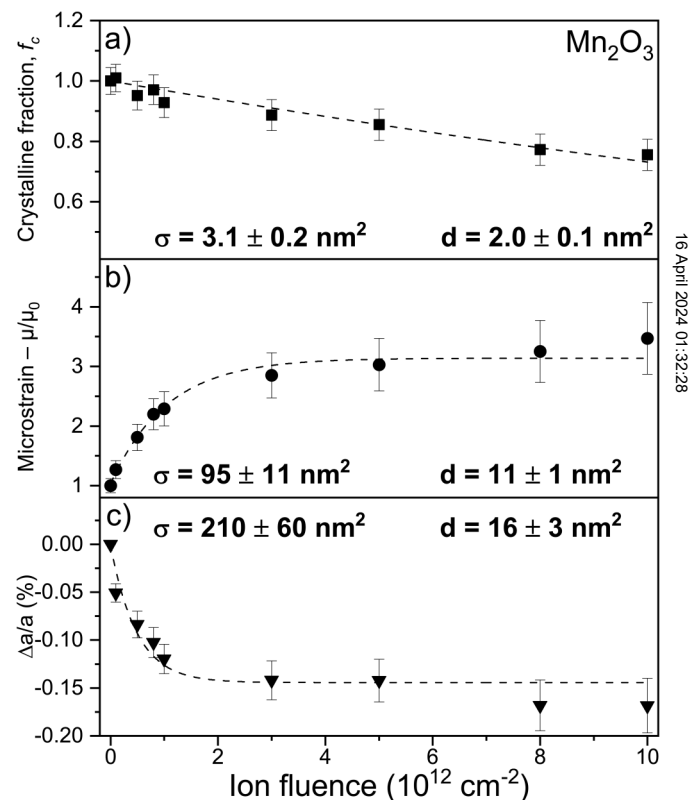

FIG. 5. (a) Stacked XRD patterns of Yb$_2$O$_3$ before and after irradiation to all ion fluences. Indices correspond to X-type (Im3m) diffraction maxima (red) and to C-type (Ia$\bar{3}$) diffraction maxima (black). The inset highlights subtle shifts of the most intense bixbyite peak with increasing ion fluence. (b) Relative unit-cell parameter of the C-type phase determined by Rietveld refinement of Yb$_2$O$_3$ XRD patterns as a function of ion fluence. The dashed line is provided to guide the eye and indicate the unit-cell parameter shift. Error bars represent the uncertainties associated with the refinements.

FIG. 6. Structural parameters of Mn$_2$O$_3$ deduced from Rietveld refinement of XRD patterns with increasing ion fluence. (a) The remaining C-type phase fraction (by weight) decreases to $\sim 80\%$ with no apparent saturation, (b) the microstrain increases and saturates, and (c) the unit-cell parameter decreases relative to the initial value, a_0, and saturates at -0.17% (contraction). The dashed lines are fits with a single-impact model, and the error bars represent the uncertainties associated with the Rietveld refinements. The cross-sectional area, σ, and the corresponding track diameters were deduced from the fits using Eq. (1).

diffuse scattering background. All diffraction maxima broaden considerably while the total integrated peak intensity diminishes with increasing ion irradiation. This sesquioxide compound is comparatively resistant to amorphization by SHI irradiation, as the refined C-type phase fraction reduces gradually to only ~80% at the maximum fluence [Fig. 6(a)]. The direct-impact model was used to fit the data and determine the cross-sectional track area and diameter using Eq. (1). The same procedure was applied as for Nd_2O_3 and Eu_2O_3, but the fit parameter b was adjusted to zero since no phase saturation is apparent up to the maximum fluence achieved. The amorphous track area and diameter were determined to be $3.1 \, nm^2$ and $2.0 \, nm$, respectively, far smaller than the values obtained for the two other amorphizable sesquioxide compositions.

The microstrain increases and the unit-cell parameter in C-type Mn_2O_3 decreases with ion fluence approaching saturation, a behavior that is well-represented by a single-impact mechanism. The relative changes in strain and unit-cell parameter proceed at a much higher rate than the amorphization process as represented by much larger cross sections. This phenomenon that has also been observed in Au-irradiated Ga_2O_3 was attributed to the production of isolated defects within a larger shell region surrounding a more highly damaged ion track core.[55] Interestingly, the unit-cell parameter does not expand under swift heavy ion irradiation but contracts with saturation at ~0.17%. This behavior is not commonly observed in amorphizable materials and may be attributed to compressive stresses from an under-dense amorphous phase or to irradiation-induced redox effects in the remaining C-type phase. Similar unit-cell contraction was previously observed in redox-sensitive binary oxides following SHI irradiation[61] and was attributed to irradiation-induced oxidation processes. Manganese has more accessible oxidation states than any other transition metal, which may present a high redox activity under extremely ionizing irradiation. If oxidation of Mn^{3+} occurs with swift heavy ions, the decrease of ionic radius may lead to unit-cell compression that overshadows possible defect-induced swelling.

IV. DISCUSSION

The precise *in situ* experimental design allowed the Cu sample holder to function as an internal standard, which was crucial for the quantitative analysis of the remaining crystalline phase and the induced amorphous phase in each sample. Using an internal standard in XRD measurements is a standard technique that has been applied extensively for quantitative phase analysis in mixed-phase polycrystalline materials since the 1940s.[53,56,62–64] Likewise, irradiation studies have regularly used crystalline peak analysis of diffraction patterns measured *in situ* to diagnose and quantify amorphization; TEM has confirmed the efficacy of this method to quantify amorphization by observation of crystalline peak attenuation.[5,12,48,54,65] Therefore, the amorphous phase fraction was determined in this study by diffraction pattern analysis of attenuated integrated peak intensities with respect to the internal copper standard diffraction peaks.

Irradiation by 946 MeV Au ions produced very similar behavior in both A-type Nd_2O_3 and C-type Eu_2O_3. Rietveld refinements using the internal copper standard showed a near-complete loss of the crystalline peak intensity which cannot be explained by

defect-induced strain broadening or a transformation to a different crystalline phase. Direct amorphization within individual ion tracks was shown to be the dominant transformation mechanism for both compositions, despite their distinct initial structures (Fig. 3). Incomplete amorphization with non-unity saturation of the amorphous fraction suggests an ion-track morphology more complex than a simple cylindrical amorphous volume in both materials. Heterogeneous ion tracks have previously been observed in $A_2B_2O_7$ pyrochlore oxides, which exhibit concentric defective regions around amorphous cores.[5] This core–shell morphology was explained by recrystallization processes that may also form epitaxial A-type (Nd_2O_3) and C-type (Eu_2O_3) shells surrounding amorphous ion track cores in Nd_2O_3 and Eu_2O_3. If crystalline shells repeatedly form, complete amorphization cannot be reached; such shells must be thin for Ln_2O_3 materials, as the direct-impact model approximates the phase fraction evolution quite well.

It has previously been observed that ion track diameters and phase transformation rates in C-type Ln_2O_3 materials decrease monotonically as the atomic number of the lanthanide increases (and thus as the ionic radius decreases); a smaller cation radius typically corresponds to greater phase stability.[14,44] This rule is confirmed for the C-type lanthanide sesquioxides in the present study, as the remaining C-type fraction is greater in Yb_2O_3 compared to Eu_2O_3 for any given fluence (e.g., 85% vs 4% at 2×10^{13} ions/cm²). However, the heightened amorphization resistance of Nd_2O_3 relative to Eu_2O_3, indicated by the smaller amorphous track diameter of Nd_2O_3, shows that the trend of increased phase stability for smaller lanthanide cations cannot be extended to A-type sequioxides (whose cations have the largest ionic radii), despite their qualitatively similar response to SHI irradiation. Furthermore, Mn_2O_3, with the smallest cation, retains a lower C-type phase fraction (80% at 10^{13} ions/cm²) compared to Yb_2O_3, indicating that this rule cannot be extended to non-lanthanide C-type oxides either. The underlying mechanism for this behavior remains unclear, but it indicates that either the Ln_2O_3 starting structure or the accessible phase space plays a role in swift heavy ion irradiations. It has been shown that C-type to B-type transformation is critical for the irradiation of most sequioxides, and the B-type phase is absent in the equilibrium phase diagram for A-type compositions such as Nd_2O_3.[14]

Interestingly, there is no evidence of ion-beam-induced B-type phase formation in any Ln_2O_3 composition under irradiation with 946 MeV Au ions. While prior SHI studies of C-type Ln_2O_3 materials reported transformations to the B-type (Ln = Sm–Er) and minor X-type (Ln = Tm–Lu) phases induced by irradiation with high ion energies (e.g., 2.2 GeV Au), lower ion energies (e.g., 185 MeV Xe) predominantly caused amorphization with minor B-type phase formation (Ln = Sm–Er) and substantial X-type formation (Ln = Tm–Lu).[14,45,46] This discrepancy in which more extensive damage results from irradiation with ions of lower energy and mass (i.e., lower dE/dx) was explained by the swift heavy ion velocity effect and associated energy density differences along ion tracks.[14,66] The distance that excited electrons travel from the ion–solid interaction region before thermalizing is proportional to the energy initially transmitted to them and thus to the ion irradiation energy. Therefore, the energy deposited to a material by high-energy ions is spread over a much larger volume than that deposited

by lower energy ions, yielding lower energy densities.[1,3] Based on the results reported here, 946 MeV Au ions have sufficiently reduced velocity compared to 2.2 GeV Au ions to generate energy densities above the threshold for amorphization. Amorphization appears to be complete for Eu_2O_3, which was not the case for the two neighboring compositions (Sm_2O_3 and Gd_2O_3) irradiated with 185 MeV Xe ions, where a minor C-type to B-type transformation was reported.[14] This can be explained by a combined effect of ion velocity and energy loss. The velocity of 946 MeV Au ions is lower than that of 2.2 GeV Au ions, resulting in an increased energy density within the track region. Compared to 185 MeV Xe ions, however, the energy loss (dE/dx) is still higher, which further increases the energy density and yields complete amorphization of Eu_2O_3.

The X-type phase, which was accessible in Yb_2O_3 by 946 MeV Au irradiation, is particularly interesting because of its highly non-equilibrium nature and predicted superionic conductivity. Neither temperature nor pressure has been demonstrated to induce the formation of an X-type phase in Yb_2O_3 or other Ln_2O_3 materials with similarly small cations. Moreover, for larger cations where the X-phase can be produced at very high temperatures, attempts to quench this phase to ambient conditions were unsuccessful. However, stresses resulting from radiation-induced defects have been shown to stabilize certain high-pressure polymorphs in oxides.[67–69] Considering that numerous high-pressure phase transformations have been reported for Ln_2O_3 materials,[31] irradiation-induced strain may play a role in stabilizing the X-type phase to ambient conditions. The fact that the X-type phase has never been reported for Yb_2O_3 in the equilibrium phase diagram emphasizes the far-from-equilibrium conditions that are accessible through SHI irradiation. Consistent results have previously been reported for Tm_2O_3 and Lu_2O_3 irradiated with energetic 185 MeV Xe ions.[14] Given that the atomic number and ionic radius of Yb are intermediate to those of Tm and Lu, the observed formation of X-type Yb_2O_3 agrees well with this prior work. Interestingly, a direct-impact transformation was proposed for Tm_2O_3 and Lu_2O_3,[14] while a multi-impact mechanism best describes the accumulation of the X-type phase in Yb_2O_3. Overlapping tracks of 946 MeV Au ions are required to reach defect concentrations necessary to drive the C-to-X transformation, which is produced directly in 185 MeV Xe ion tracks. This discrepancy may be related to the difference in the ion velocity, energy loss, or a combination of both.

Saturation of X-type phase fraction in Yb_2O_3 was determined to be about 15% for 946 MeV Au ions (Fig. 4), unlike previous results that have found no such X-type saturation in Tm_2O_3 and Lu_2O_3 by direct impact. This finding depends disproportionally on the highest fluence data point, and further irradiation experiments to much higher fluences are required to unambiguously confirm that X-type transformation saturates at such a low phase fraction. If accurate, this finding is intriguing as it suggests that a pure X-type phase cannot be produced by this particular ion species and energy. Similarly, to the incomplete amorphization of Eu_2O_3, this behavior can be explained by a core–shell morphology. While the X-type phase forms by track overlap, a C-type shell is continuously formed. Given the low saturation value, the shell size must dominate the cross-sectional area of ion tracks. An X-type phase has also been shown to form in Er_2TiO_5 at extreme pressure[70] and in $Gd_2Zr_2O_7$ under simultaneous pressure and SHI irradiation.[71] Park et al. reported only a partial recovery to ambient conditions for Er_2TiO_5,[70] while Lang et al. confirmed a complete quenching to atmospheric pressure for $Gd_2Zr_2O_7$.[71] Further work should evaluate whether synergistic effects of pressure and irradiation are required for complete X-type formation and recovery. Once experimental protocols have been established and a sufficient quantity of the X-type phase is available for broadband dielectric spectroscopy measurements, its unique ionic properties should be explored.

Since Mn_2O_3 exhibits the smallest cation radius among the studied C-type materials, it is expected to be most stable under SHI irradiation. Despite its high resistance to amorphization relative to Eu_2O_3, Mn_2O_3 retains less of its C-type phase than Yb_2O_3 and amorphizes somewhat. Fitting a direct-impact model to the phase fractions indicates a small amorphous core only 2 nm in diameter, surrounded by a strained C-type region (11 nm diameter), which is part of a larger defective C-type region (16 nm diameter). Mn_2O_3 may reasonably be expected to form an X-type phase, as is typical of Ln_2O_3 materials with smaller cations, yet Mn_2O_3 forms no detectable X-type under the same irradiation conditions for which Yb_2O_3 transforms. Instead, minor amorphization is evident and the relative stability of the C-type phase under irradiation with 946 MeV Au ions is intermediate of Eu_2O_3 and Yb_2O_3. This behavior may be related to the 23% lower ion energy loss of Mn_2O_3 (~37 keV/nm) relative to Yb_2O_3 (~48 keV/nm) resulting from the lower density of the former. The induced energy density may not be sufficiently high to form the X-type phase or cause more substantial amorphization as shown for Eu_2O_3. The distinct behavior of Mn_2O_3 may also suggest that irradiation-induced modifications in sesquioxides depend not only on cation size but also on the electronic structure. X-type phase formation may be specific to A_2O_3 materials with lanthanide cations. Different effects may come into play for other cations, such as redox behavior, which is absent for many lanthanide elements. Reduction and oxidation processes can be triggered by highly ionizing radiation,[9] and partial oxidation in Mn_2O_3 from Mn^{3+} to Mn^{4+} can explain the unusual unit-cell contraction (Fig. 6). Possible changes in stoichiometry and excess oxygen may render the highly anion-deficient X-type phase inaccessible in this sesquioxide composition.

V. CONCLUSIONS

Irradiation of Nd_2O_3, Eu_2O_3, Yb_2O_3, and Mn_2O_3 with 946 MeV Au ions over a range of fluences and subsequent XRD characterization provided new insight into the radiation responses and compositional trends in various sesquioxides. The structural responses were analyzed in vacuo at the beamline, which allowed the analysis of an air-sensitive A-type phase for the first time with a dense array of fluence steps to determine detailed phase-transformation mechanisms. The crystalline-to-amorphous transformation proceeds by a direct-impact mechanism for A-type Nd_2O_3 and C-type Eu_2O_3. Amorphization consistent with a direct-impact mechanism is also evident in C-type Mn_2O_3, but at a much slower rate than in Nd_2O_3 and Eu_2O_3. The formation of an X-type phase, as expected for small cation ionic radii, was not

16 April 2024 01:32:28

confirmed in Mn_2O_3 up to the highest fluence studied. Amorphous track diameters in Nd_2O_3, Eu_2O_3, and Mn_2O_3 are approximately 8.9, 14.1, and 2.0 nm, respectively, and saturation of amorphous phase fractions below 100% is indicative of a core–shell morphology. The A-type phase with the largest cation ionic radius is relatively more radiation tolerant than a C-type phase with medium-sized cations. C-type Mn_2O_3 is much more resistant against amorphization than the other two amorphizable compositions, which can be explained by electronic structure effects. Partial oxidation may be induced in this non-lanthanide sesquioxide by extremely ionizing radiation, leading to an unusual unit-cell contraction. The C-type sesquioxide with the smallest lanthanide cation (Yb_2O_3) undergoes a C-to-X phase transformation by a multi-impact mechanism with saturation at ~15% X-type phase. This agrees well with earlier work reporting the formation of this phase in similar lanthanide sesquioxides. However, the results shown here differ from the prior analysis with respect to the observed saturation of the X-type phase fraction below 20% and the type of transformation mechanism (multi-impact in this study vs direct impact in previous studies). Further research is needed to fully understand the formation and quenching of this far-from-equilibrium phase by swift heavy ion irradiation and a possible synthesis route for a phase pure X-type material at ambient conditions. Neutron scattering experiments coupled with impedance spectroscopy can then be used to elucidate details regarding the oxygen ions' structural role in the irradiated material, obtain additional information about the predicted superionic conductivity properties, and assess potential use in solid oxide fuel cell electrolytes.

DATA AVAILABILITY

The data that support the findings of this study are available from the corresponding author upon reasonable request.

REFERENCES

[1]N. Itoh, D. M. Duffy, S. Khakshouri, and A. M. Stoneham, J. Phys.: Condens. Matter **21**(47), 474205 (2009).

[2]A. V. Lankin, I. V. Morozov, G. E. Norman, S. A. Pikuz, Jr., and I. Y. Skobelev, Phys. Rev. E **79**(3), 036407 (2009).

[3]D. M. Duffy, S. L. Daraszewicz, and J. Mulroue, Nucl. Instrum. Methods Phys. Res. Sect. B **277**, 21–27 (2012).

[4]M. Lang, R. Devanathan, M. Toulemonde, and C. Trautmann, Curr. Opin. Solid State Mater. Sci. **19**(1), 39–48 (2015).

[5]M. Lang, J. Lian, J. M. Zhang, F. X. Zhang, W. J. Weber, C. Trautmann, and R. C. Ewing, Phys. Rev. B **79**(22), 9 (2009).

[6]C. L. Tracy, M. Lang, F. X. Zhang, S. Park, R. I. Palomares, and R. C. Ewing, Prog. Nucl. Energy **104**, 342–358 (2018).

[7]C.-H. Chen, C. L. Tracy, C. Wang, M. Lang, and R. C. Ewing, Appl. Phys. Lett. **112**(7), 073904 (2018).

[8]M. Jublot, F. Paumier, F. Pailloux, B. Lacroix, E. Leau, P. Guerin, M. Marteau, M. Jaouen, R. J. Gaboriaud, and D. Imhoff, Thin Solid Films **515**(16), 6385–6390 (2007).

[9]W. E. Cureton, R. I. Palomares, C. L. Tracy, E. C. O'Quinn, J. Walters, M. Zdorovets, R. C. Ewing, M. Toulemonde, and M. Lang, J. Nucl. Mater. **525**, 83–91 (2019).

[10]R. I. Palomares, J. Shamblin, C. L. Tracy, J. Neuefeind, R. C. Ewing, C. Trautmann, and M. Lang, J. Mater. Chem. A **5**(24), 12193–12201 (2017).

[11]K. E. Sickafus, H. Matzke, T. Hartmann, K. Yasuda, J. A. Valdez, P. Chodak III, M. Nastasi, and R. A. Verrall, J. Nucl. Mater. **274**, 66 (1999).

[12]F. Lu, J. Wang, M. Lang, M. Toulemonde, F. Namavar, C. Trautmann, J. Zhang, R. C. Ewing, and J. Lian, Phys. Chem. Chem. Phys. **14**(35), 12295–12300 (2012).

[13]M. Jubera, J. Villarroel, A. Garcia-Cabanes, M. Carrascosa, J. Olivares, F. Agullo-Lopez, A. Mendez, and J. B. Ramiro, Appl. Phys. B: Lasers Opt. **107**(1), 157–162 (2012).

[14]C. L. Tracy, M. Lang, F. Zhang, C. Trautmann, and R. C. Ewing, Phys. Rev. B **92**(17), 174101 (2015).

[15]J. Lian, L. Wang, J. Chen, K. Sun, R. C. Ewing, J. Matt Farmer, and L. A. Boatner, Acta Mater. **51**(5), 1493–1502 (2003).

[16]A. Benyagoub, Phys. Rev. B **72**(9), 094114 (2005).

[17]R. J. Gaboriaud, M. Jublot, F. Paumier, and B. Lacroix, Nucl. Instrum. Methods Phys. Res. Sect. B **310**, 6–9 (2013).

[18]I. P. Jain and G. Agarwal, Surf. Sci. Rep. **66**(3–4), 77–172 (2011).

[19]M. C. Ridgway, F. Djurabekova, and K. Nordlund, Curr. Opin. Solid State Mater. Sci. **19**(1), 29–38 (2015).

[20]F. Druon, M. Velazquez, P. Veber, S. Janicot, O. Viraphong, G. Buse, M. A. Ahmed, T. Graf, D. Rytz, and P. Georges, Opt. Lett. **38**(20), 4146–4149 (2013).

[21]C. J. Saraceno, O. H. Heckl, C. R. E. Baer, M. Golling, T. Sudmeyer, K. Beil, C. Krankel, K. Petermann, G. Huber, and U. Keller, Opt. Express **19**(21), 20288–20300 (2011).

[22]K. H. Goh, A. Haseeb, and Y. H. Wong, Mater. Sci. Semicond. Process **68**, 302–315 (2017).

[23]H. J. Osten, J. P. Liu, and H. J. Müssig, Appl. Phys. Lett. **80**(2), 297–299 (2002).

[24]H. X. Dai, C. F. Ng, and C. T. Au, Appl. Catal. A-Gen. **202**(1), 1–15 (2000).

[25]Z. Taherian, M. Yousefpour, M. Tajally, and B. Khoshandam, Int. J. Hydrogen Energy **42**(26), 16408–16420 (2017).

[26]L. Zhou, Z. Gu, X. Liu, W. Yin, G. Tian, L. Yan, S. Jin, W. Ren, G. Xing, W. Li, X. Chang, Z. Hu, and Y. Zhao, J. Mater. Chem. **22**(3), 966–974 (2012).

[27]J. C. Yin, C. R. Li, Y. B. Yang, W. Y. Hu, H. Liu, and Y. Z. Shao, RSC Adv. **6**(76), 72836–72844 (2016).

[28]M. Durazzo, F. B. V. Oliveira, E. F. Urano de Carvalho, and H. G. Riella, J. Nucl. Mater. **400**(3), 183–188 (2010).

[29]J. Lian, L. M. Wang, S. X. Wang, J. Chen, L. A. Boatner, and R. C. Ewing, Phys. Rev. Lett. **87**(14), 145901 (2001).

[30]J. Coutures, A. Rouanet, R. Verges, and M. Foex, J. Solid State Chem. **17**(1–2), 171–182 (1976).

[31]F. J. Manjon, J. A. Sans, J. Ibanez, and A. L. D. Pereira, Crystals **9**(12), 32 (2019).

[32]B. P. Uberuaga and K. E. Sickafus, Comput. Mater. Sci. **103**, 216–223 (2015).

[33]P. Aldebert, A. J. Dianoux, and J. P. Traverse, J. Phys. **40**(10), 1005–1012 (1979).

[34]S. Hull, Rep. Prog. Phys. **67**(7), 1233–1314 (2004).

16 April 2024 01:32:28

[35]B. C. H. Steele, Mater. Sci. Eng. B-Solid State Mater. Adv. Technol. **13**(2), 79–87 (1992).

[36]T. Atou, K. Kusaba, Y. Tsuchida, W. Utsumi, T. Yagi, and Y. Syono, Mater. Res. Bull. **24**(9), 1171–1176 (1989).

[37]L. Bai, J. Liu, X. Li, S. Jiang, W. Xiao, Y. Li, L. Tang, Y. Zhang, and D. Zhang, J. Appl. Phys. **106**(7), 073507 (2009).

[38]S. Jiang, J. Liu, C. Lin, L. Bai, Y. Zhang, X. Li, Y. Li, L. Tang, and H. Wang, Solid State Commun. **169**, 37–41 (2013).

[39]S. Jiang, J. Liu, C. Lin, X. Li, and Y. Li, J. Appl. Phys. **113**(11), 113502 (2013).

[40]G. Adachi and N. Imanaka, Chem. Rev. **98**(4), 1479–1514 (1998).

[41]R. J. Gaboriaud, F. Paumier, M. Jublot, and B. Lacroix, Nucl. Instrum. Methods Phys. Res. Sect. B **311**, 86–92 (2013).

[42]M. Tang, P. Lu, J. A. Valdez, and K. E. Sickafus, Philos. Mag. **86**(11), 1597–1613 (2006).

[43]S. Bilgen, G. Sattonnay, C. Grygiel, I. Monnet, P. Simon, and L. Thome, Nucl. Instrum. Methods Phys. Res. Sect. B **435**, 12–18 (2018).

[44]M. Tang, P. Lu, J. A. Valdez, and K. E. Sickafus, J. Appl. Phys. **99**(6), 063514 (2006).

[45]M. Lang, F. Zhang, J. Zhang, C. L. Tracy, A. B. Cusick, J. VonEhr, Z. Chen, C. Trautmann, and R. C. Ewing, Nucl. Instrum. Methods Phys. Res. Sect. B **326**, 121–125 (2014).

[46]G. Sattonnay, S. Bilgen, L. Thome, C. Grygiel, I. Monnet, O. Plantevin, C. Huet, S. Miro, and P. Simon, Phys. Status Solidi B-Basic Solid State Phys. **253**(11), 2110–2114 (2016).

[47]M. Tabuchi, K. Ado, H. Kobayashi, H. Kageyama, C. Masquelier, A. Kondo, and R. Kanno, J. Electrochem. Soc. **145**(4), L49–L52 (1998).

[48]M. Lang, F. Zhang, W. Li, D. Severin, M. Bender, S. Klaumünzer, C. Trautmann, and R. C. Ewing, Nucl. Instrum. Methods Phys. Res. Sect. B **286**, 271–276 (2012).

[49]M. Nagao, H. Hamano, K. Hirata, R. Kumashiro, and Y. Kuroda, Langmuir **19**(22), 9201–9209 (2003).

[50]J. F. Ziegler, M. D. Ziegler, and J. P. Biersack, Nucl. Instrum. Methods Phys. Res. Sect. B **268**(11–12), 1818–1823 (2010).

[51]H. M. Rietveld, J. Appl. Crystallogr. **2**, 65–71 (1969).

[52]B. H. Toby and R. B. Von Dreele, J. Appl. Crystallogr. **46**, 544–549 (2013).

[53]H. P. Klug and L. Alexander, *X-ray Diffraction Procedures: For Polycrystalline and Amorphous Materials*, 2nd ed. (John Wiley & Sons, New York, 1974).

[54]G. Sattonnay, S. Moll, L. Thome, C. Decorse, C. Legros, P. Simon, J. Jagielski, I. Jozwik, and I. Monnet, J. Appl. Phys. **108**(10), 103512 (2010).

[55]C. L. Tracy, M. Lang, D. Severin, M. Bender, C. Trautmann, and R. C. Ewing, Nucl. Instrum. Methods Phys. Res. Sect. B **374**, 40–44 (2016).

[56]W. C. Mosley, J. Am. Ceram. Soc. **54**(10), 475–479 (1971).

[57]B. E. Warren, J. Am. Ceram. Soc. **17**, 249–254 (1934).

[58]D. Balzar, N. Audebrand, M. R. Daymond, A. Fitch, A. Hewat, J. I. Langford, A. Le Bail, D. Louër, O. Masson, C. N. McCowan, N. C. Popa, P. W. Stephens, and B. H. Toby, J. Appl. Crystallogr. **37**, 911–924 (2004).

[59]W. J. Weber, Nucl. Instrum. Methods Phys. Res. Sect. B **166**, 98–106 (2000).

[60]G. Sattonnay, C. Grygiel, I. Monnet, C. Legros, M. Herbst-Ghysel, and L. Thomé, Acta Mater. **60**(1), 22–34 (2012).

[61]W. F. Cureton, R. I. Palomares, J. Walters, C. L. Tracy, C.-H. Chen, R. C. Ewing, G. Baldinozzi, J. Lian, C. Trautmann, and M. Lang, Acta Mater. **160**, 47–56 (2018).

[62]H. P. Klug, L. Alexander, and E. Kummer, Anal. Chem. **20**(7), 607–609 (1948).

[63]F. H. Chung, J. Appl. Crystallogr. **7**(6), 519–525 (1974).

[64]B. Ohtani, O. O. Prieto-Mahaney, D. Li, and R. Abe, J. Photochem. Photobiol. A-Chem. **216**(2–3), 179–182 (2010).

[65]G. Sattonnay, N. Sellami, L. Thome, C. Legros, C. Grygiel, I. Monnet, J. Jagielski, I. Jozwik-Biala, and P. Simon, Acta Mater. **61**(17), 6492–6505 (2013).

[66]A. Meftah, F. Brisard, J. M. Costantini, M. Hage-Alli, J. P. Stoquert, F. Studer, and M. Toulemonde, Phys. Rev. B **48**(2), 920–925 (1993).

[67]D. Simeone, G. Baldinozzi, D. Gosset, S. Lecaer, L. Mazerolles, I. Monnet, and S. Bouffard, Nucl. Instrum. Methods Phys. Res. Sect. B **266**(12–13), 3023–3026 (2008).

[68]B. Schuster, F. Fujara, B. Merk, R. Neumann, T. Seidl, and C. Trautmann, Nucl. Instrum. Methods Phys. Res. Sect. B **277**, 45–52 (2012).

[69]C. Gibert-Mougel, F. Couvreur, J. M. Costantini, S. Bouffard, F. Levesque, S. Hémon, E. Paumier, and C. Dufour, J. Nucl. Mater. **295**(1), 121–125 (2001).

[70]S. Park, D. R. Rittman, C. L. Tracy, K. W. Chapman, F. X. Zhang, C. Park, S. N. Tkachev, E. O'Quinn, J. Shamblin, M. Lang, W. L. Mao, and R. C. Ewing, Inorg. Chem. **57**(4), 2269–2277 (2018).

[71]M. Lang, F. Zhang, J. Zhang, J. Wang, B. Schuster, C. Trautmann, R. Neumann, U. Becker, and R. C. Ewing, Nat. Mater. **8**(10), 793–797 (2009).

16 April 2024 01:32:28